

**Boosting Electrochemical Water Splitting via Ternary NiMoCo Hybrid Nanowire Arrays**

Journal:	<i>Journal of Materials Chemistry A</i>
Manuscript ID	TA-ART-11-2018-011250.R1
Article Type:	Paper
Date Submitted by the Author:	16-Dec-2018
Complete List of Authors:	Hu, Kailong; University of Tsukuba, Graduate School of Pure and Applied Sciences Wu, Mingxing; University of Tsukuba Hinokuma, Satoshi; Kumamoto University, Graduate School of Science and Technology Ohto, Tatsuhiko; Osaka University, Wakisaka, Mitsuru ; Toyama Prefectural University Fujita, J; Tsukuba University, Institute of Applied Physics Ito, Yoshikazu; University of Tsukuba,



ARTICLE

Boosting Electrochemical Water Splitting via Ternary NiMoCo Hybrid Nanowire Arrays

Received 00th January 20xx,
Accepted 00th January 20xx

Kailong Hu,^a Mingxing Wu,^a Satoshi Hinokuma,^{b, c, d} Tatsuhiko Ohto,^{e, *} Mitsuru Wakisaka,^{d, f} Jun-ichi Fujita,^a and Yoshikazu Ito^{a, d, *}

DOI: 10.1039/x0xx00000x

www.rsc.org/

Hydrogen production by way of electrochemical water splitting is a technology with the potential to meet the growing worldwide demand for sustainable and clean energy. However, the development of cost-effective catalysts to replace noble metals, such as platinum or ruthenium, remains a crucial point for large-scale hydrogen production. This study presents the synthesis of a transition non-noble metal-based ternary NiMoCo hybrid nanowire array as an efficient bifunctional electrocatalyst for overall water splitting in a 1.0 M KOH electrolyte. The catalyst exhibits a low cell voltage of 1.56 V to achieve a water-splitting current density of 10 mA cm⁻² together with long-term stability with only 5% of the initial current lost after 100 hours. The X-ray absorption spectroscopy confirms the addition of Co to the binary Ni-Mo system results in highly mixed chemical binding with modulated electronic structures. Density functional theory (DFT) calculations reveal the Co atoms on the ternary alloy become catalytically active sites and facilitate adsorption of intermediates by ensuring preferable interactions between the reactants and the catalyst surface in comparison to the binary counterpart. This work provides a new direction along which to activate binary alloys to further enhance their catalytic abilities on overall water splitting.

1 Introduction

Electrolytic water splitting is one of the most promising approaches to meet the booming global demand for clean and sustainable hydrogen energy.^{1,2} State-of-the-art technologies generally use Pt and RuO₂ to accelerate the two half reactions of the water-splitting process, i.e., the hydrogen evolution reaction (HER) at the cathode and the oxygen evolution reaction (OER) at the anode, due to the sluggish kinetics of both processes.³ However, the high cost of noble metal catalysts and the scarcity of resources hinder the penetration rate of this technology on a wide scale to realize the hydrogen society.

In recent decades, numerous types of electrode materials have been developed to explore replacements of noble metal catalysts by earth-abundant catalysts for the electrochemical

HER/OER process, including non-noble metal alloys/oxides (NiMo, NiFe, FeCo),⁴⁻¹⁰ metallic nitrides (WN, MoN),¹¹⁻¹³ transition metal dichalcogenides MX₂ (M=Mo, W, Re, Fe, Co, Ni; X=S, Se),¹⁴⁻²¹ metallic phosphides (NiP, CoP, NiMoP),²²⁻²⁶ and metal-free carbon materials (C₃N₄, doped-graphene).²⁷⁻³² Among the various electrocatalysts, transition metal-based composites have been considered desirable overall water-splitting catalysts, due to the remarkable HER/OER activity, which is similar to that of Pt-group materials, and which is explained by the particular d-band electronic structure.^{2,33-35} However, the catalytic activity of binary alloys is often limited and desirable electrode designs of non-noble metal alloys are required for efficient multi-functional catalysts. More recently, some ternary transition metal catalysts, which show bifunctional activity superior to that of binary metal catalysts, have been developed. The electronic structure of these catalysts is determined by the strong synergistic effects of each transition metal, which promotes the optimal interaction between reaction intermediates and the catalyst surface during the HER/OER process according to the Sabatier principle.³⁶⁻⁴¹ For instance, ternary NiCoFe alloy nanosheets exhibited superior HER/OER performance in comparison to their binary counterparts (NiFe, CoFe, NiCo) because the electronic state is tuned toward optimal binding of the reaction intermediates⁴² on the Volcano plot.⁴³ Moreover, integration of the optimal catalytic activity⁴⁴ of the HER of NiMo and the OER of NiCo could contribute to bifunctional HER/OER catalysts as similarly reported ternary catalyst⁴⁵ although its molecular-based catalytic mechanism is unclear.

^a Institute of Applied Physics, Graduate School of Pure and Applied Sciences, University of Tsukuba, 1-1-1 Tennodai, Tsukuba 305-8571, Japan.

^b Department of Applied Chemistry and Biochemistry, Graduate School of Science and Technology, Kumamoto University, 2-39-1 Kurokami, Kumamoto 860-8555, Japan.

^c International Research Organization for Advanced Science and Technology, 2-39-1 Kurokami, Kumamoto 860-8555, Japan.

^d PRESTO, Japan Science and Technology Agency, Saitama 332-0012, Japan

^e Graduate School of Engineering Science, Osaka University, 1-3 Machikaneyama, Toyonaka 560-8531, Japan

^f Graduate School of Engineering, Toyama Prefectural University, 5180 Kurokawa, Imizu, Toyama 939-0398, Japan

*E-mail address: ito.yoshikazu.ga@u.tsukuba.ac.jp; ohto@molelectronics.jp

Electronic Supplementary Information (ESI) available: See

DOI: 10.1039/x0xx00000x

Based on the above-mentioned advantages of ternary alloy catalysts, the elements in ternary alloys are considered to strongly interact with each other. They undergo rearrangements of their bond coordination, which results in a more energetically unstable state (highly mixed chemical binding state) and a catalytically active state as reported.⁴⁶⁻⁴⁸ Thus, ternary alloys can be expected to be catalytically active with respect to the HER/OER process.

Herein, we report ternary NiMoCo alloy nanowire arrays on Ni foam as bifunctional catalysts for overall water splitting in an alkaline electrolyte. The NiMoCo coated on Ni foam has a hierarchical porous structure with the micro-sized pores belonging to the Ni foam as primary pores and the nano-sized pores in the nanowires as secondary ones. The Ni foam and its primary pores facilitate mass transport from the electrolyte into the electrode surface and H₂/O₂ gas diffusion from the catalyst surface to the outside. Simultaneously, the nanopores in the nanowire afford a high exposure of catalytically active sites to the electrolyte. Moreover, the tuning of the surface electronic state by the ternary elements brings highly mixed chemical binding state in the NiMoCo alloy, which is confirmed by X-ray absorption spectroscopy. Such a state is expected to enhance the efficiency of these materials as bifunctional electrocatalysts.^{48, 49} The catalytic reaction mechanism and Gibbs free energies of adsorption of intermediates on the NiMoCo ternary alloy were investigated by density functional theory (DFT) calculations. Such hierarchical porous architectures and the catalytically active surface electronic state enable the ternary NiMoCo alloy catalyst to not only achieve superior bifunctional performances than those of binary counterparts in terms of the overall water-splitting process, but also paves a new design route for versatile and designable ternary catalysts.

2 Experimental

2.1 Preparation of Ni/Mo/Co oxides coated on Ni foam

As-received Ni foam (1.0 cm², Celmet No. 8, Sumitomo Electric) was cleaned by acetone, 1.0 M HNO₃ solution, and ultrapure water (resistivity: 18.2 MΩ cm), and then dried under vacuum. The dried Ni foams were placed into a 50 ml Teflon coated stainless autoclave with 1.5 mmol NiCl₂·6H₂O (98% purity, Wako), 1.5 mmol Na₂MoO₄·2H₂O (99% purity, Wako), 0.75 mmol Co(NO₃)₂·6H₂O (98% purity, Wako), and 30 mL ultrapure water. A standard hydrothermal procedure was carried out at 150 °C for 6 hours. After cooling down to room temperature naturally, the obtained Ni/Mo/Co oxides coated on Ni foam (NF@Ni/Mo/CoO_x) was washed by ultrapure water several times and sequentially dried under vacuum.

2.2 Preparation of NiMoCo alloy nanowires coated on Ni foam

The NF@Ni/Mo/CoO_x was loaded on a corundum boat, and then inserted into a quartz tube (φ30×φ27×1000 mm) furnace. The reduction of Ni/Mo/CoO_x on the Ni foam surface was performed at 500 °C for 2 hours under a mixed atmosphere of H₂ (100 sccm) and Ar (200 sccm). After the reduction process, NiMoCo alloy nanowires coated on Ni foam were obtained. The NiMoCo samples with various Co concentrations were

similarly synthesized with different amounts of Co reagent. Meanwhile, the binary counterparts, such as NiMo, MoCo and NiCo coated on Ni foam were also synthesized via the same procedures with different reagents. For example, 1.5 mol NiCl₂·6H₂O and 1.5 mol Na₂MoO₄·2H₂O were used for NiMo sample synthesis, whereas 1.5 mol Na₂MoO₄·2H₂O and 0.75 mol Co(NO₃)₂·6H₂O were used for MoCo sample preparation. The loading amount of NiMoCo, NiMo, MoCo, and NiCo on a 1.0 cm² Ni foam was measured as 3 mg, 2.8 mg, 2.8 mg, and 2.6 mg (±0.2 mg), respectively, after the annealing processes.

2.3 Preparation of Pt/C and Ru₂O coated on Ni foam

6 mg Pt/C (10 wt%, Sigma-Aldrich) or Ru₂O (74.4–77.5% as Ru, Wako) powder was dispersed in a solution mixed with 400 μL of ethanol, 80 μL of ultrapure water, and 20 μL of Nafion (5% DE521 CS type, Wako), and then ultrasonication was performed for 30 min to achieve a highly dispersed ink. 250 μL of ink was pipetted on the surface of a 1.0 cm² Ni foam. The loading amount of Pt/C or Ru₂O after drying was 3.0±0.2 mg, respectively.

2.4 Preparation of NiMoCo alloy nanowires coated on carbon cloth

Synthesis was similarly performed with the process of NiMoCo coated on Ni foam, whereas Ni foam was replaced with carbon cloth as substrates (CC@NiMoCo). The loading amount of NiMoCo on a 1.0 cm² carbon cloth after the annealing processes was 3.2±0.2 mg.

2.5 Imaging and spectroscopic characterization

The morphology and microstructure of as-synthesized catalysts were characterized by a scanning electron microscope (SEM, JEOL JSM-4300), a transmission electron microscope (JEOL JEM-2100F and JEM-ARM200F), and JEM-ARM200F equipped EDS analysis (SDD Type, Detection surface area 30 mm², Solid angle 0.26 sr).

2.6 Structural characterization

The structural characterizations were analyzed by X-ray diffraction (XRD) using a RIGAKU SmartLab 9MTP diffractometer with a 9.0 kW rotating anode generator (Cu Kα₁ radiation; λ=1.5406 Å). The surface chemical states were investigated by X-ray photoelectron spectroscopy (XPS, AXIS ultra DLD, Shimadzu) with Al Kα and X-ray monochromator. Co, Ni, and Mo K-edge XAFS (X-ray absorption fine structure) were performed on the BL9C station of the Photon Factory (PF), High Energy Accelerator Research Organization (KEK). Measurement samples were prepared by depositing NiMoCo alloy nanowires and NiMo counterpart on carbon cloth to exclude any possible influence from metal substrates. The XAFS spectra were recorded at ambient temperature in transmission mode using an ionization chamber (filled with 100% N₂ for Co, 100% N₂ for Ni, and 50% N₂/Ar for Mo) for the incident beam, another chamber (filled with 85% N₂/Ar for Co, 75% N₂/Ar for Ni, and 100% Ar for Mo) for the transmitted beam, and a Si (111) double-crystal monochromator. Reference samples without foils were mixed with boron nitride (BN) powder to achieve an appropriate absorbance at the edge energy. The XAFS data were processed using the IFEFFIT software package (Athena and Artemis). Surface areas of samples were measured by nitrogen absorption and desorption measurements with Brunauer–Emmett–Teller (BET) theory using a BELSORP-MAX (BEL JAPAN. INC) at 77.0 K. The horizontal axis was normalized with the vapor pressure of nitrogen (P₀) at 77.0 K (=

0.101 MPa). Samples were heated at 120 °C under vacuum for 24 hours before measurements.

2.7 Electrochemical characterizations

The electrochemical workstation (Biologic, VSP-300) was used for electrochemical measurements. HER and OER tests were carried out in a three-electrode system, where a graphite rod, a Ag/AgCl electrode, as-prepared samples, and 1.0 M KOH solution (pH \approx 13.9) was served as count electrode, reference electrode, working electrode, and electrolyte, respectively. The pH value of electrolyte was recorded before test, and the Ag/AgCl reference electrode was calibrated using a Pt wire as working electrode before use. The electrolytes were Ar-saturated and O₂-saturated for HER and OER tests, respectively. The electrode potential was automatically *iR*-compensated with the Ohmic resistance. All potentials were calculated with respect to RHE using the equation: $E(\text{RHE}) = E(\text{Ag}/\text{AgCl}) + 0.0591 \times \text{pH} + 0.197$. The polarization curves were achieved via a sweep rate of 1.0 mV s⁻¹ to decrease the capacitive background. The electrochemical impedance spectra (EIS) was collected by AC impedance spectroscopy with frequencies ranging from 100 kHz to 1 Hz. The double-layer capacitance, C_{dl} , was estimated on the basis of cyclic voltammetry (CV) tested between +700 and +900 mV (vs. RHE) with various sweep rates from 30 to 70 mV/s.⁵⁰ The C_{dl} was measured by plotting the $\Delta j = j_{\text{a}} - j_{\text{c}}$ at +800 mV (vs. RHE) against the sweep rates.^{7, 51} The C_{dl} value is equal to half of the slope value.⁵² The overall water splitting tests were performed in 1.0 M KOH solution using a two-electrode electrolyzer, and the as-obtained samples were used as both anode and cathode with a fixed electrode distance of 2.5 cm. All the data for two-electrode electrolyzer were collected without *iR* compensation.

2.8 DFT calculation

The first-principles calculations were performed with the VASP code. We used the projected augmented wave (PAW) method. For the exchange and core-functional, we used the Perdew-Burke-Ernzerhof (PBE) functional. The plane wave energy cutoff was set to 400 Ry. The dispersion correction was included via the Grimme's D3 (BJ) method. Calculation details are in the supporting information.

3 Results and discussion

The fabrication process of the NiMoCo alloy nanowires and their deposition on Ni foam (NF@NiMoCo) entailed the reduction of the coated Ni/Mo/Co oxide nanofibers on the Ni foam (Fig. 1a). First, a standard hydrothermal method was employed to synthesize the Ni/Mo/Co oxide nanofibers on Ni foam (NF@Ni/Mo/CoO_x). Second, NF@Ni/Mo/CoO_x was reduced at 500 °C for 2 hours under a mixed atmosphere of Ar and H₂ to obtain the NiMoCo nanowires. Scanning electron microscopy (SEM) images presented that these nanowires gathered and formed a flower-like array on Ni foam (Fig. 1c

and 1d). The SEM image in Fig. S1a showed the porous structure of Ni foam (pore diameter \approx 200 μm ; primary pores). The specific surface areas of NF@NiMoCo and the Ni foam substrate were measured by conducting nitrogen absorption and desorption measurements based on Brunauer-Emmett-Teller (BET) theory.⁵³ The surface areas were determined to be 6.48 m² g⁻¹ and 0.30 m² g⁻¹, respectively (Fig. S2). The binary counterparts with the combinations NiMo, MoCo, and NiCo coated on Ni foam (NF@NiMo, NF@MoCo, and NF@NiCo) were similarly characterized (Fig. S1 and S2).

The atomic structures of the NiMoCo nanowires were investigated by transmission electron microscopy (TEM). The nanowires were constructed with open and nanoporous architectures with a pore diameter of approximately 20 nm (secondary pores) in each nanowire (Fig. 1e and 1f). The high-resolution TEM (HRTEM) image (Fig. 1g) presented that the various kinds of lattice fringes with distances of 0.18, 0.21, 0.22, and 0.24 nm correspond to the (027) and (116) planes of NiMo₂Co, and the (041) and (231) planes of NiMo, respectively. This suggests the co-existence of NiMo₂Co and NiMo nanoregions in the nanowires. The corresponding selected area electron diffraction (SAED) pattern showed (116) and (027) planes for NiMo₂Co, and (113), (041), and (025) planes for NiMo indexed according to the reported X-ray diffraction (XRD) data (Fig. 1h), which also supports the co-presence of NiMo₂Co and NiMo. Indeed, energy-dispersive X-ray spectroscopy (EDS) mapping (Fig. 1i) confirmed that the nanowire constituted Ni, Mo, Co, and O with a highly homogeneous distribution without obviously localized Ni/Mo/Co oxidized species.

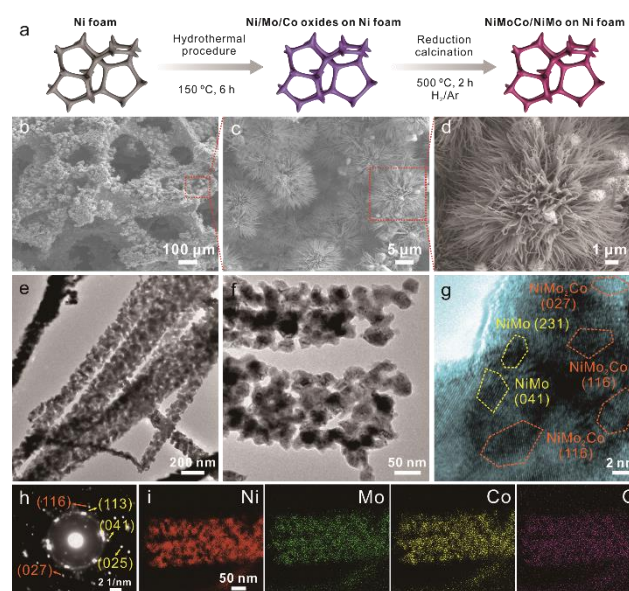


Fig. 1 (a) Fabrication process of NF@NiMoCo. (b-d) Surface morphologies of NiMoCo alloy nanowire arrays coated on Ni foam. (e) Overview, (f) enlarged TEM images, (g) HRTEM image, and (h) SAED pattern of the NiMoCo alloy nanowires. (i) EDS mapping of Ni, Mo, Co, and O in a nanowire.

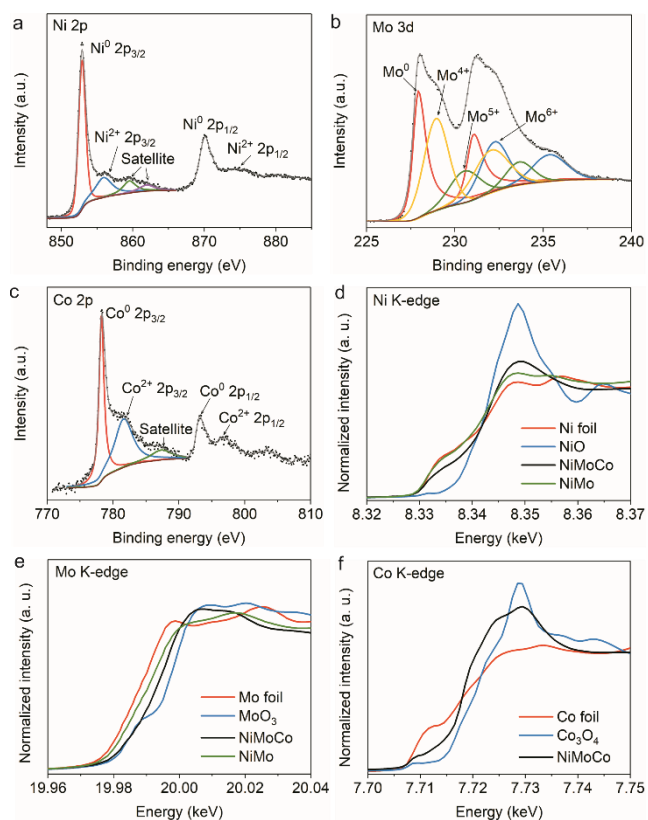


Fig. 2 High-resolution XPS spectra of (a) Ni 2p, (b) Mo 3d, and (c) Co 2p of NF@NiMoCo. K-edge XANES spectra of NF@NiMoCo and NF@NiMo: (d) Ni, (e) Mo, and (f) Co.

The structures and chemical states of NF@NiMoCo were analyzed with XRD and X-ray photoelectron spectroscopy (XPS). The XRD pattern (Fig. S3a) revealed major peaks located at 43.7° and 51.1° , which were assigned to the (116) and (027) planes of NiMo₂Co (JCPDS 09–0298). The peaks at 35.8° , 36.9° , and 40.8° were indexed to the (032), (231), and (041) planes of NiMo (JCPDS 48–1745). Additionally, peaks attributable to Ni foam (JCPDS 65–2865) and NiMoO₄ (JCPDS 33–0948) were also observed. The XRD pattern of NiMoCo coated on carbon cloth (CC@NiMoCo), which was recorded to exclude the influence of the Ni foam substrate signals, also showed the (116) and (027) planes of NiMo₂Co (Fig. S3b). The XRD peaks of the (116) and (027) planes corresponded to the HRTEM and SAED observations. Moreover, the XPS spectrum of NF@NiMoCo (Fig. S4) confirmed the surface state of Ni, Mo, and Co. The high-resolution Ni 2p spectrum (Fig. 2a) comprised peaks at 852.9 and 856.0 eV that were assigned to Ni⁰ and Ni²⁺.⁵⁴ The Mo 3d spectrum (Fig. 2b) could be deconvoluted into Mo⁰ (227.9 and 231.1 eV) as well as Mo oxides (Mo⁴⁺: 229 and 232.1 eV; Mo⁵⁺: 230.6 and 233.7 eV; Mo⁶⁺: 232.3 and 235.4 eV).⁵⁵ The Co 2p spectrum (Fig. 2c) could be fitted by two spin orbit doublets, including Co⁰ (778.3 and 793.2 eV) and Co²⁺ (781.7 and 796.8 eV).⁴⁰ The chemical compositions of Ni/Mo/Co on the surface was determined as 33.8 at.% for Ni, 47.9 at.% for Mo, and 18.3 at.% for Co. The XPS spectra of NF@NiMo, NF@MoCo, and NF@NiCo were similarly characterized (Fig. S5).

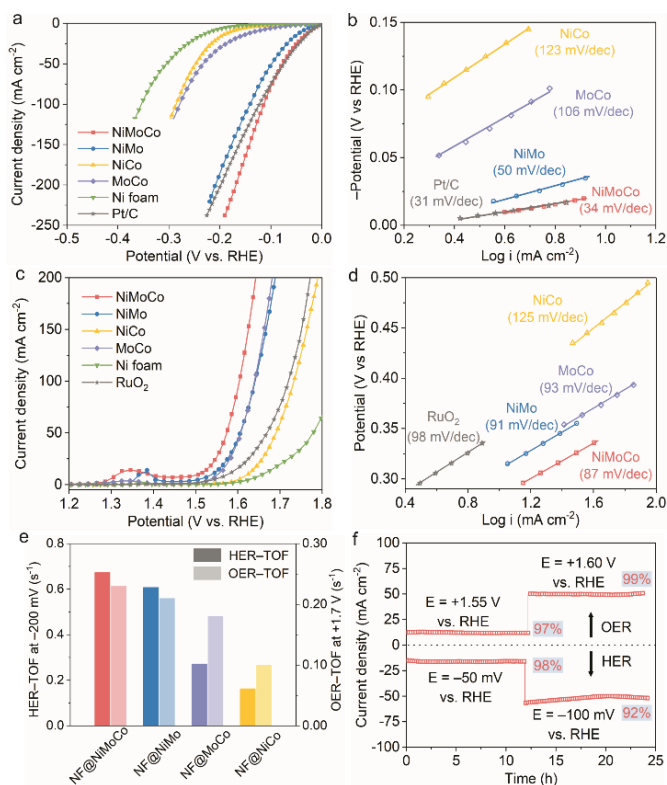


Fig. 3 (a) HER polarization curves and (b) Tafel plots of NF@NiMoCo, NF@NiMo, NF@MoCo, NF@NiCo as compared with commercial NF@Pt/C. (c) OER polarization curves and (d) Tafel plots of NF@NiMoCo, NF@NiMo, NF@MoCo, NF@NiCo as compared with commercial NF@RuO₂. Sweep rate: 1 mV s⁻¹. (e) TOF values of HER and OER at -200 mV and $+1.7$ V vs. RHE. (f) Long-term durability test of NF@NiMoCo at various potentials.

To understand the influence of introducing Co on electron modulation, we further characterized the NiMoCo and NiMo samples through X-ray absorption near-edge structure (XANES). In the respective K-edge spectra of Ni and Mo (Fig. 2d and 2e), the electronic states of these two elements in the NiMoCo sample became an electron deficient state (between the metallic and oxidized states) in comparison to those of the NiMo sample. Additionally, the Co K-edge spectra also showed that the electronic state of Co in the NiMoCo alloy becomes electron deficient in comparison to that of Co foil (metal) (Fig. 2f). Thus, the addition of Co introduces strong electron modulation to the NiMoCo alloy. Moreover, the extended X-ray absorption fine structure (EXAFS) was subjected to Fourier transform and analyzed (Fig. S6). The NiMoCo alloy showed wider and broadened radial distances ranging from 2.0 to 3.0 Å in comparison to NiMo (Fig. S6a). This means that the addition of Co atoms rearranges various kinds of bond coordination in the NiMoCo ternary alloy and the complicated bond coordination results in an energetically unstable (catalytically active) state.^{46–48} The electron deficient state on NiMoCo alloy surface with the complicated bond coordination (Fig. 2 and S6) could be beneficial for electrochemical redox reactions.^{46, 48, 49}

The catalytic performance of the as-synthesized electrocatalysts as cathodes (HER) and anodes (OER) was examined in 1.0 M KOH with *iR* compensation in a three-electrode system, respectively. The best Co atomic concentration in the ternary NiMoCo sample coated on Ni

foam was investigated among samples with Co 10.8 at.%, 19.3 at.%, 29.4 at.%, and 35.9 at.% through SEM, XPS and CV measurements (Fig. S7 and S8), and the Co 19.3 at.% sample with best performances was employed for further studies (Supporting discussion 1#). The HER polarization curves (Fig. 3a) were investigated to compare the catalytic performances of the Ni foam substrate (pristine Ni foam), NF@NiMo, NF@MoCo, NF@NiCo, NF@NiMoCo and commercial 10 wt.% Pt/C coated on Ni foam (NF@Pt/C) as cathodes with a loading amount of approximately 3 mg cm⁻². The NF@NiMoCo exhibited a superior HER activity, exceeding those of binary counterparts under the same loading amount. The cathode potential at a current density of 10 mA cm⁻² ($\eta_{10\text{-HER}}$) was 22, 23, 39, 130, and 177 mV vs. the reversible hydrogen electrode (RHE) for NF@Pt/C, NF@NiMoCo, NF@NiMo, NF@MoCo, and NF@NiCo, respectively. Noticeably, the onset potential of NF@NiMoCo was as low as that of the benchmark NF@Pt/C. The turnover frequency (TOF), which affords a direct comparison of intrinsic catalytic activities, of NF@NiMoCo achieved the highest value of 0.67 s⁻¹ in comparison to its binary counterparts (0.16–0.60 s⁻¹) at –200 mV vs. RHE (Fig. 3e).

Tafel plots, double-layer capacitance (C_{dl}), and electrochemical impedance spectroscopy (EIS) were used to examine the mechanism of the HER process. The NF@NiMoCo revealed a small Tafel slope of 34 mV dec⁻¹, which is almost comparable to that of NF@Pt/C, whereas the binary catalysts exhibited higher values ranging from 50 to 123 mV dec⁻¹ (Fig. 3b). The Tafel slope suggests the Volmer–Heyrovsky process is predominant in the case of NF@NiMoCo.⁵¹ The C_{dl} was measured via a cyclic voltammetry (CV) test at different sweep rates in the non-faradaic current region (Fig. S9a). NF@NiMoCo shows the C_{dl} value of 5.25 mF cm⁻¹, and other counterparts with the value ranging from 0.83 to 8.78 mF cm⁻¹ (Fig. S9b). The electrochemical surface areas (ECSAs), which were partly estimated by the C_{dl} values. Noticeably, with a lower ECSA value than that of NF@NiMo, the superior catalytic activity of NF@NiMoCo is probably attributed to the surface energetically unstable state. Moreover, EIS was used to understand the HER kinetics at an electrode potential of –200 mV vs. RHE. Nyquist plots of the catalysts (Fig. S10a) revealed semicircles. The R_{ct} value, which represents the charge-transfer resistance between the electrolyte and catalyst, is 0.82 Ω for NF@NiMoCo. This value is lower than that of the other binary catalysts (1.3–2.6 Ω) and indicates a faster charge-transfer ability. As summarized in Fig. S11 and Table S1, the HER activity of NF@NiMoCo surpassed most of reported water-splitting catalysts.

Other than the remarkable HER activity, the OER performance of the NF@NiMoCo as anodes was also investigated as compared with that of binary catalysts and commercial RuO₂ coated on Ni foam (NF@RuO₂). The NF@NiMoCo demonstrated the overpotential as low as 277 mV was required to achieve a current density of 10 mA cm⁻² ($\eta_{10\text{-OER}}$) (Fig. 3c). This performance exceeded that of the binary counterparts (308–393 mV) (Table S2). The peak at approximately 1.35 V vs. RHE is reported as Ni oxidation.⁵⁶

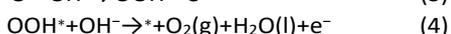
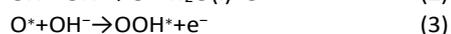
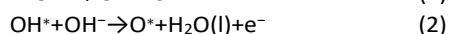
Meanwhile, the TOF at 1.7 V vs. RHE was 0.23 s⁻¹ for NF@NiMoCo. In comparison, other binary catalysts showed lower values ranging from 0.1 to 0.21 s⁻¹ (Fig. 3e). The Tafel slope presented the lowest value of 87 mV dec⁻¹ for NF@NiMoCo, whereas the other samples showed larger values of 91–125 mV dec⁻¹ (Fig. 3d). Moreover, the R_{ct} of NF@NiMoCo in the OER process afforded a small value of 1.4 Ω at overpotential of 350 mV vs. RHE (Fig. S10b). Both the small Tafel slope and R_{ct} value suggest that NF@NiMoCo has fast reaction kinetics, which would support high OER activity.

The long-term durability of NF@NiMoCo was evaluated for both the HER and OER processes by carrying out chronoamperometry (CA) measurements. In the HER process, the NF@NiMoCo was tested at potentials (vs. RHE) of –50 and –100 mV for 24 hours, and more than 90% of the initial current density was retained (Fig. 3f); additionally, the $\eta_{10\text{-HER}}$ value increased by 5 mV after 1000 CV cycles (Fig. S12a). In the OER process, the catalyst maintained its performance at levels of more than 97% and 99% at +1.55 V and +1.60 V (vs. RHE) after a 24-h durability test (Fig. 3f). After 1000 CV cycles, the $\eta_{10\text{-OER}}$ was increased by only 4 mV (Fig. S12b). The morphology and structure of the NF@NiMoCo catalyst after HER/OER durability tests were examined by SEM, TEM, XRD, XPS, and XANES (Fig. S13–S16). The NF@NiMoCo catalyst after the test kept the original morphologies but the chemical state was changed in the surface redox process during the HER/OER test. The NF@NiMoCo catalyst after HER tests kept the metallic state, while it showed the oxides/hydroxides state after OER tests. Chemical leaching was further tested by using inductively coupled plasma optical emission spectrometry (ICP–OES). The catalysts on Ni foam retained (Fig. S13) with slight dissolution, as confirmed by a time-dependent ICP leaching check (Fig. S17 and supporting discussion 2#). Thus, the morphology and chemical state of electrodes was preserved for keeping long-term catalytic activity. Moreover, the NF@NiMoCo electrode was measured in a highly concentrated KOH electrolyte (30 wt.%), in which its high catalytic performance and chemical stability were similarly retained (Fig. S18, S19, and supporting discussion 3#).

To elucidate the catalytic mechanism by Co atom additions responsible for the outstanding bifunctional activity of NF@NiMoCo, we performed DFT calculations using the PBE+D3(BJ) theory under periodic boundary conditions, with initial coordinates of NiMo₂Co(116), NiMo₂Co(027), and NiMo(100) (δ -phase) as a reference (Fig. S20–S22). The overall HER mechanism in alkaline media was thought to involve a H adsorption stage ($\text{H}_2\text{O} + \text{e}^- \rightarrow \text{H}^* + \text{OH}^-$) and a H₂ generation stage ($2\text{H}^* \rightarrow \text{H}_2$ or $\text{H}^* + \text{H}_2\text{O} + \text{e}^- \rightarrow \text{OH}^- + \text{H}_2$).⁵⁴ Herein, HER activity was evaluated based on the Gibbs free energies for H* adsorption (ΔG_{H^*}), which are summarized in Fig. 4a. Negative ΔG_{H^*} values were observed for NiMo₂Co(027), which significantly delays the desorption process of intermediates. The ΔG_{H^*} values for NiMo(100) (–0.23 eV) and NiMo₂Co(116) (–0.47 eV) were closer to that of highly efficient Pt catalyst (–0.09 eV)⁵⁷ and MoS₂ (–0.36 to +0.39 eV)⁵⁸, indicating that NiMo(100) and NiMo₂Co(116) contribute to the HER process. In addition, according to the calculation of the hydrogen-metal

binding energy (HBE) on the catalyst surface, the NiMoCo with (110) plane shows an HBE value very close to that of Pt (111).³⁶ As the NiMoO₄ species in NF@NiMoCo does not contribute to the HER/OER activity (Fig. S23 and supporting discussion 4#), proper planes in NiMo and NiMo₂Co play an important role in the enhancement of HER performances. Moreover, the molecular adsorption sites of H* intermediates on the surface of NiMo₂Co(116) and NiMo₂Co(027) were investigated (Fig. S24). It was found that the Co atoms on both NiMo₂Co(116) and NiMo₂Co(027) become the H* adsorption sites.

In the OER process, the reaction mechanism for 3d transition metal-based (oxy)hydroxide catalysts in alkaline electrolyte has been reported and the reaction process undergoes the following steps:⁵⁹



where * represents that the intermediates of OH, O and OOH are adsorbed on an active site on the catalyst surface. To evaluate the OER activity of the NiMo₂Co alloy, we examined the adsorption mechanism of intermediate (Fig. 5, S25 and S26) and calculated the Gibbs free energy for each intermediate after surface oxidation (Fig. 4b, Table 1 and Table S3).

The individual molecular adsorption configuration on each plane was examined and the preferable adsorption sites were found on the flat plane as a top site and on the step-like high-index plane as a bridge site (Fig. S26). The NiMo₂Co(116) surface is constructed with Mo-rich configurations (Fig. S21), and the surface is very flat. According to DFT results, the OH*, O* and OOH* species adsorbed on the Mo top sites and the Mo-Co bridge site. Especially, the OOH* species form an O₂-like bridge such as one oxygen on Co atom and the other oxygen on Mo atom (Fig. S25). This indicated that the (116) plane does not have preferable adsorption sites for the OOH* species. Conversely, the NiMo₂Co(027) surface is constructed with Co-rich configuration (Fig. 5a), and Mo top sites on the flat plane and Mo-Co bridge sites near the step-like plane mainly contribute to the adsorption of intermediates (Fig. 5a and S26). In addition, the NiMo(100) surface as a reference is constructed with Ni and Mo atoms (Fig. 5b) and Ni hollows as bridge sites contribute to the adsorption of intermediates (Fig. 5b).

As the preferred molecular adsorption sites are the top and bridge sites, the molecular adsorption site dependence of ΔG was investigated. The resulting Gibbs free energy diagram of each OER process on NiMo₂Co(116) and NiMo₂Co(027) under zero potential and 1.23 V (vs. RHE) was plotted in comparison to NiMo(100) (Fig. 4b). The $|\Delta G|$ of top and bridge sites on the NiMo₂Co(116) and the top site on the NiMo₂Co(027) surface at

each reaction steps demonstrated larger value than the bridge site on the NiMo₂Co(027) surface under 1.23 V (vs. RHE) (Table 1), which indicated the NiMo₂Co(027) surface enhances the intermediate adsorption process. In other words, the Gibbs free energy close to zero benefits the reduction of activation energy for each reaction steps, and thus the bridge sites on NiMo₂Co(027) are preferable as active sites than the top sites. In addition, the formation of OH* and O* species at the step (1) and (2) are easily accessible, whereas the rate controlling step under both 0 V and 1.23 V (vs. RHE) is the conversion from O* to OOH* species at step (3) due to the very strong O* adsorption. Especially, the difference value between ΔG_{O^*} and ΔG_{OOH^*} of NiMo₂Co(027) bridge site under 1.23 V (vs. RHE) was lowest (1.669 eV) with the positive ΔG_{OOH^*} in comparison to that of NiMo(100) value (1.695 eV) with the negative ΔG_{OOH^*} and that of NiMo₂Co(116) bridge site's value (3.117 eV) with the positive ΔG_{OOH^*} , indicating the NiMo₂Co(027) promotes the overall OER process. Thus, the most preferable adsorption site in our NiMoCo ternary alloy is the Mo-Co bridge site on the NiMo₂Co(027) plane for the OER process, and the Co atoms on the NiMo₂Co(027) surface also play an important role as catalytically active sites.

Table 1 Summary of Gibbs adsorption free energy values under 1.23 V (vs. RHE)

	G(OH*), eV	G(O*), eV	G(OOH*), eV
NiMo ₂ Co(027) (top site)	-1.040	-2.111	-0.687
NiMo ₂ Co(027) (bridge site)	-0.432	-1.460	0.209
NiMo ₂ Co(116) (top site)	-1.527	-2.084	-0.724
NiMo ₂ Co(116) (bridge site)	-1.013	-2.523	0.594
NiMo100	-0.813	-1.817	-0.122

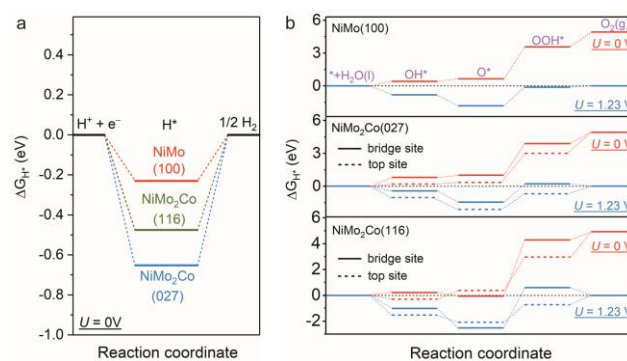


Fig. 4 DFT-calculated Gibbs free energies of (a) H* adsorption on NiMo₂Co(116) and NiMo₂Co(027) during HER process. (b) Gibbs free energies of OH*, O* and OOH* adsorption on NiMo₂Co(116) and NiMo₂Co(027) during OER process in comparison to NiMo(100).

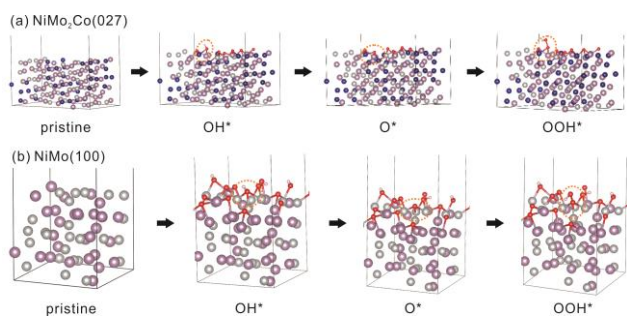


Fig. 5 DFT-calculated molecular adsorption mechanism of OER process on (a) $\text{NiMo}_2\text{Co}(027)$ (bridge site) and (b) $\text{NiMo}(100)$. The silver, violet, blue, red and small pink balls represent Ni, Mo, Co, O, and H atoms, respectively. Orange circles show adsorption sites of each intermediates. Red balls without orange circles represent the oxygen atoms of self-generated oxides/hydroxides on the catalyst surface during OER process.

In the chemical and morphological viewpoints, the self-generated Ni/Mo/Co oxide/hydroxide species on the catalyst surface during OER process confirmed by XRD (Fig. S14) also contributed to the enhancement of OER performance. XPS and XANES spectra also indicated the dominated state on catalyst surface transformed from a metallic state into an oxidation state with high chemical valences (Fig. S15 and S16) after the OER tests. The oxide/hydroxide species could provide preferable adsorption and desorption free energies for the reaction intermediates (OH^* and OOH^*) compared to the metallic species.^{37, 55, 60} Moreover, the Ni foam substrate provides fast electron transport for the catalytic reactions occurred on NiMoCo nanowires (Fig. S27, S28 and supporting discussion 5#) Additionally, the hierarchical porous structure promotes not only the mass transport of the active species in the electrolyte to the catalyst surface, but also the quick diffusion of generated gas bubbles. Meanwhile, the secondary nanopores on the NiMoCo nanowires afford a large surface area and further promote the electrocatalytic activity for overall water-splitting performances.

Finally, we have demonstrated the overall water-splitting performance using as-synthesized catalysts as the cathodic and anodic electrodes in 1.0 M KOH without iR compensation using a two-electrode system. A low cell voltage of +1.56 V was necessary to obtain 10 mA cm^{-2} ($E_{10\text{-water splitting}}$) by the NF@NiMoCo couple electrodes, exhibiting activity superior to that of NF@NiMo (+1.62 V), NF@MoCo (+1.69 V), NF@NiCo (+1.78 V), Ni foam (+1.87 V), and $\text{NF@Pt/C}||\text{NF@RuO}_2$ (+1.67 V) couples (Fig. 5a). The performance of the NF@NiMoCo couple electrodes exceeded that of the major reported non-noble metal-based bifunctional water-splitting catalysts (Table S4). Hydrogen and oxygen bubbles were observed to be generated on the surfaces of two electrodes (inset of Fig. 5c). The H_2 and O_2 gases generated at a constant current of 20 mA were collected to calculate the faradaic efficiency (Fig. 5b). The gas volume corresponded well with the theoretically calculated volume, achieving almost 100% faradaic efficiency. Furthermore, the long-term stability of NF@NiMoCo for overall water splitting was tested at a cell voltage of +1.6 V (Fig. 5c). The water-splitting cell retained 95% of its initial current density, and the $E_{10\text{-water splitting}}$ was only increased by 19 mV after 100 hours (Fig. 5d).

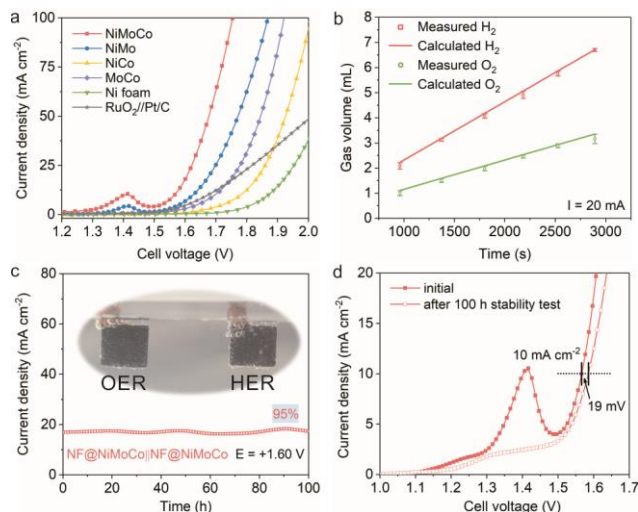


Fig. 6 (a) Polarization curves measured using a couple of the same electrocatalysts as anodes and cathodes. Sweep rate: 1 mV s^{-1} . (b) Experimentally measured and theoretically calculated gas volumes of H_2 and O_2 produced during overall water splitting of NF@NiMoCo . (c) Chronoamperometry test of a couple of NF@NiMoCo electrodes at a cell voltage of +1.6 V. Inset: optical image of the two-electrode electrolysis system. (d) Polarization curves before and after the durability test of 100 h.

4 Conclusion

In summary, we successfully synthesized NiMoCo hybrid nanowire arrays supported on Ni foam with hierarchical porous structures as bifunctional non-noble metal catalysts for efficient overall water splitting. This ternary NiMoCo catalyst, using as both the anode and cathode, exhibited superior activity to that of its binary counterparts, such as NiMo , MoCo , and NiCo . The addition of Co atom to the binary alloy resulted in a highly mixed chemical binding state, which plays an important role in modulating the surface electronic state, optimizing Gibbs free energies of intermediate adsorption, and boosting both HER and OER processes in comparison to the binary alloy. The DFT calculations also indicated the Co atoms on the surface of $\text{NiMo}_2\text{Co}(027)$ plane are preferable active sites for intermediates adsorption during HER/OER process. The NF@NiMoCo achieved a low cell voltage of 1.56 V for a water-splitting current density of 10 mA cm^{-2} together with excellent stability (5% initial current loss) for 100 hours. The designable ternary alloy in combination with desirable bifunctional activities can be expected to open a feasible path to achieve multi-functional catalysts to meet the social demands for various electrocatalytic reactions.

Conflicts of interest

There are no conflicts to declare.

Acknowledgements

We thank Ms. Kazuyo Omura at the Institute for Material Research in Tohoku University for XPS measurements. The

XAFS experiments were performed at BL9C with the approval of PF, KEK (Proposal No. 2016G527). This work was sponsored by JST-PRESTO "Creation of Innovative Core Technology for Manufacture and Use of Energy Carriers from Renewable Energy" (JPMJPR1541, JPMJPR1444); JSPS Grant-in-Aid for Scientific Research on Innovative Areas "Discrete Geometric Analysis for Materials Design": Grant Number JP18H04477; JSPS KAKENHI Grant Number JP18K14174; World Premier International Research Center Initiative (WPI), MEXT, Japan;

NIMS microstructural characterization platform as a program of "Nanotechnology Platform" of the MEXT, Japan.; University of Tsukuba Basic Research Support Program Type S, the Open Facility, Research Facility Center for Science and Technology, University of Tsukuba, the TEPCO Memorial Foundation. K. L. Hu was supported by the Japanese Government (MONBUKAGAKUSHO: MEXT) Scholarship and the Kato Foundation for Promotion of Science (KS-3032). T. Ohto acknowledges the supercomputer of ACCMS, Kyoto University.

Notes and references

- X. X. Zou and Y. Zhang, *Chem. Soc. Rev.*, 2015, **44**, 5148–5180.
- S. Anantharaj, S. R. Ede, K. Sakthikumar, K. Karthick, S. Mishra, S. Kundu, *ACS Catal.*, 2016, **6**, 8069–8097.
- J. Wang, F. Xu, H. Y. Jin, Y. Q. Chen and Y. Wang, *Adv. Mater.*, 2017, **29**, 1605838.
- F. Song and X. L. Hu, *Nat. Commun.*, 2014, **5**, 4477.
- J. Q. Tian, N. Y. Cheng, Q. Liu, X. P. Sun, Y. Q. He and A. M. Asiri, *J. Mater. Chem. A*, 2015, **3**, 20056–20059.
- K. L. Hu, S. Jeong, M. Wakisaka, J.-i. Fujita and Y. Ito, *Metals*, 2018, **8**, 83.
- L. Yu, H. Q. Zhou, J. Y. Sun, F. Qin, F. Yu, J. M. Bao, Y. Yu, S. Chen and Z. F. Ren, *Energy Environ. Sci.*, 2017, **10**, 1820–1827.
- K. L. Hu, T. Ohto, L. H. Chen, J. H. Han, M. Wakisaka, Y. Nagata, J.-i. Fujita and Y. Ito, *ACS Energy Lett.* 2018, **3**, 1539–1544.
- C. C. McCrory, S. Jung, I. M. Ferrer, S. M. Chatman, J. C. Peters and T. F. Jaramillo, *J. Am. Chem. Soc.*, 2015, **137**, 4347–4357.
- Y. Y. Ji, L. Yang, X. Ren, G. W. Cui, X. L. Xiong and X. P. Sun, *ACS Sustainable Chem. Eng.*, 2018, **6**, 9555–9559.
- H. J. Yan, C. G. Tian, L. Wang, A. P. Wu, M. C. Meng, L. Zhao and H. G. Fu, *Angew. Chem. Int. Ed.*, 2015, **54**, 6325–6329.
- J. F. Xie, S. Li, X. D. Zhang, J. J. Zhang, R. X. Wang, H. Zhang, B. C. Pan and Y. Xie, *Chem. Sci.*, 2014, **5**, 4615–4620.
- Z. X. Yin, Y. Sun, C. L. Zhu, C. Y. Li, X. T. Zhang and Y. J. Chen, *J. Mater. Chem. A*, 2017, **5**, 13648–13658.
- D. S. Kong, J. J. Cha, H. T. Wang, H. R. Lee and Y. Cui, *Energy Environ. Sci.*, 2013, **6**, 3553–3558.
- Q. P. Lu, Y. F. Yu, Q. L. Ma, B. Chen and H. Zhang, *Adv. Mater.*, 2016, **28**, 1917–1933.
- C. Tang, N. Y. Cheng, Z. H. Pu, W. Xing and X. P. Sun, *Angew. Chem. Int. Ed.*, 2015, **127**, 9483–9487.
- L.-L. Feng, G. T. Yu, Y. Y. Wu, G.-D. Li, H. Li, Y. H. Sun, T. Asefa, W. Chen and X. X. Zou, *J. Am. Chem. Soc.*, 2015, **137**, 14023–14026.
- N.-T. Suen, S.-F. Hung, Q. Quan, N. Zhang, Y.-J. Xu and H. M. Chen, *Chem. Soc. Rev.*, 2017, **46**, 337–365.
- D. Voiry, H. Yamaguchi, J. W. Li, R. Silva, D. C. B. Alves, T. Fujita, M. W. Chen, T. Asefa, V. B. Shenoy, G. Eda and M. Chhowalla, *Nat. Mater.*, 2013, **12**, 850–855.
- T. Fujita, Y. Ito, Y. W. Tan, H. Yamaguchi, D. Hojo, A. Hirata, D. Voiry, M. Chhowalla and M. W. Chen, *Nanoscale*, 2014, **6**, 12458–12462.
- W. Y. Wang, L. Yang, F. L. Qu, Z. A. Liu, G. Du, A. M. Asiri, Y. D. Yao, L. Chen and X. P. Sun, *J. Mater. Chem. A*, 2017, **5**, 16585–16589.
- E. J. Popczun, J. R. McKone, C. G. Read, A. J. Biacchi, A. M. Wiltrout, N. S. Lewis and R. E. Schaak, *J. Am. Chem. Soc.*, 2013, **135**, 9267–9270.
- Q. Liu, J. Q. Tian, W. Cui, P. Jiang, N. Y. Cheng, A. M. Asiri and X. P. Sun, *Angew. Chem. Int. Ed.*, 2014, **126**, 6828–6832.
- J. Q. Tian, Q. Liu, A. M. Asiri and X. P. Sun, *J. Am. Chem. Soc.*, 2014, **136**, 7587–7590.
- Y. Y. Ji, L. Yang, X. Ren, G. W. Cui, X. L. Xiong and X. P. Sun, *ACS Sustainable Chem. Eng.*, 2018, **6**, 11186–11189.
- X.-D. Wang, H.-Y. Chen, Y.-F. Xu, J.-F. Liao, B.-X. Chen, H.-S. Rao, D.-B. Kuang and C.-Y. Su, *J. Mater. Chem. A*, 2017, **5**, 7191–7199.
- Y. Zheng, Y. Jiao, Y. H. Zhu, L. H. Li, Y. Han, Y. Chen, A. J. Du, M. Jaroniec and S. Z. Qiao, *Nat. Commun.*, 2014, **5**, 3783.
- Y. Ito, W. T. Cong, T. Fujita, Z. Tang and M. W. Chen, *Angew. Chem. Int. Ed.*, 2015, **54**, 2131–2136.
- Y. Ito, Y. H. Shen, D. Hojo, Y. Itagaki, T. Fujita, L. H. Chen, T. Aida, Z. Tang, T. Adschiri and M. W. Chen, *Adv. Mater.*, 2016, **28**, 10644–10651.
- Y. Zheng, Y. Jiao, L. H. Li, T. Xing, Y. Chen, M. Jaroniec and S. Z. Qiao, *ACS Nano*, 2014, **8**, 5290–5296.
- L. L. Zhang, J. Xiao, H. Y. Wang and M. H. Shao, *ACS Catal.* 2017, **7**, 7855–7865.
- Y. Jiao, Y. Zheng, K. Davey and S. Z. Qiao, *Nat. Energy*, 2016, **1**, 16130.
- Y. Jiao, Y. Zheng, M. Jaroniec and S. Z. Qiao, *Chem. Soc. Rev.*, 2015, **44**, 2060–2086.
- R. Subbaraman, D. Tripkovic, K.-C. Chang, D. Strmcnik, A. P. Paulikas, P. Hirunsit, M. Chan, J. Greeley, V. Stamenkovic and N. M. Markovic, *Nat. Mater.*, 2012, **11**, 550–557.
- V. R. Stamenkovic, B. S. Mun, M. Arenz, K. J. Mayrhofer, C. A. Lucas, G. F. Wang, P. N. Ross and N. M. Markovic, *Nat. Mater.*, 2007, **6**, 241–247.
- W. C. Sheng, A. P. Bivens, M. Myint, Z. B. Zhuang, R. V. Forest, Q. R. Fang, J. G. Chen and Y. S. Yan, *Energy Environ. Sci.*, 2014, **7**, 1719–1724.
- B. Zhang, X. L. Zheng, O. Voznyy, R. Comin, M. Bajdich, M. García-Melchor, L. L. Han, J. X. Xu, M. Liu, L. R. Zheng, F. P. Arquer, C. T. Dinh, F. J. Fan, M. J. Yuan, E. Yassitepe, N. Chen, M. Regier, P. F. Liu, Y. H. Li, P. D. Luna, A. Janmohamed, H. L. Xin, H. G., Yang, A. Vojvodic and E. H. Sargent, *Science*, 2016, **352**, 333–337.
- W. Ahn, M. G. Park, D. U. Lee, M. H. Seo, G. P. Jiang, Z. P. Cano, F. M. Hassan and Z. W. Chen, *Adv. Func. Mater.*, 2018, 1802129.
- A. J. Medford, A. Vojvodic, J. S. Hummelshøj, J. Voss, F. Abild-Pedersen, F. Studt, T. Bligaard, A. Nilsson and J. K. Nørskov, *J. Catal.*, 2015, **328**, 36–42.
- X. Q. Ji, B. P. Liu, X. Ren, X. F. Shi, A. M. Asiri and X. P. Sun, *ACS Sustainable Chem. Eng.*, 2018, **6**, 4499–4503.
- Z. Q. Wang, X. Ren, Y. L. Luo, L. Wang, G. W. Cui, F. Y. Xie, H. J. Wang, Y. Xie and X. P. Sun, *Nanoscale*, 2018, **10**, 12302–12307.
- A.-L. Wang, H. Xu and G.-R. Li, *ACS Energy Lett.*, 2016, **1**, 445–453.
- V. Stamenkovic, B. S. Mun, K. J. Mayrhofer, P. N. Ross, N. M. Markovic, J. Rossmeisl, J. Greeley and J. K. Nørskov, *Angew. Chem. Int. Ed.*, 2006, **118**, 2963–2967.

- 44 Y. Ito, H. Ohta, Y. M. Yamada, T. Enoki and Y. Uozumi, *Chem. Commun.*, 2014, **50**, 12123–12126.
- 45 J.-W. Wang, Y.-F. Wang, J.-G. Zhang, Y.-L. Yu, G.-G. Zhou, L. Cheng, L.-S. Wang and Z. Z. Fang, *Rare Metals*, 2015, **34**, 802–807.
- 46 T. Takeguchi, T. Yamanaka, K. Asakura, E. N. Muhamad, K. Uosaki and W. Ueda, *J. Am. Chem. Soc.*, 2012, **134**, 14508–14512.
- 47 J. W. Yeh, S. K. Chen, S. J. Lin, J. Y. Gan, T. S. Chin, T. T. Shun, C. H. Tsau and S. Y. Chang, *Adv. Eng. Mater.*, 2004, **6**, 299–303.
- 48 J. Staszak-Jirkovský, C. D. Malliakas, P. P. Lopes, N. Danilovic, S. S. Kota, K.-C. Chang, B. Genorio, D. Strmcnik, V. R. Stamenkovic, M. G. Kanatzidis and N. M. Markovic, *Nat. Mater.*, 2016, **15**, 197–203.
- 49 X. E. Liu, W. Liu, M. Ko, M. Park, M. G. Kim, P. Oh, S. Chae, S. Park, A. Casimir, G. Wu and J. Cho, *Adv. Func. Mater.*, 2015, **25**, 5799–5808.
- 50 J. Z. Huang, J. C. Han, R. Wang, Y. Y. Zhang, X. J. Wang, X. H. Zhang, Z. H. Zhang, Y. M. Zhang, B. Song and S. Jin, *ACS Energy Lett.*, 2018, **3**, 1698–1707.
- 51 W. C. Sheng, H. A. Gasteiger and S.-H. Yang, *J. Electrochem. Soc.*, 2010, **157**, B1529–B1536.
- 52 Y. Yang, L. N. Dang, M. J. Shearer, H. Y. Sheng, W. J. Li, J. Chen, P. Xiao, Y. H. Zhang, R. J. Hamers and S. Jin, *Adv. Energy Mater.*, 2018, **8**, 1703189.
- 53 E. P. Barrett, L. G. Joyner and P. P. Halenda, *J. Am. Chem. Soc.*, 1951, **73**, 373–380.
- 54 J. Zhang, T. Wang, P. Liu, Z. Q. Liao, S. H. Liu, X. D. Zhuang, M. W. Chen, E. Zschech and X. L. Feng, *Nat. Commun.*, 2017, **8**, 15437.
- 55 I. C. Man, H.-Y. Su, F. Calle-Vallejo, H. A. Hansen, J. I. Martínez, N. G. Inoglu, J. Kitchin, T. F. Jaramillo, J. K. Nørskov and J. Rossmeisl, *ChemCatChem*, 2011, **3**, 1159–1165.
- 56 M. W. Louie and A. T. Bell, *J. Am. Chem. Soc.*, 2013, **135**, 12329–12337.
- 57 P. T. Wang, X. Zhang, J. Zhang, S. Wan, S. J. Guo, G. Lu, J. L. Yao and Q. X. Huang, *Nat. Commun.*, 2017, **8**, 14580.
- 58 C. Tsai, F. A.-Pedersen and J. K. Nørskov, *Nano Lett.*, 2014, **14**, 1381–1387.
- 59 M. Gong, W. Zhou, M.-C. Tsai, J. G. Zhou, M. Y. Guan, M.-C. Lin, B. Zhang, Y. F. Hu, D.-Y. Wang, J. Yang, S. J. Pennycook, B.-J. Hwang and H. J. Dai, *Nat. Commun.*, 2014, **5**, 4695.
- 60 J. Jiang, F. F. Sun, S. Zhou, W. Hu, H. Zhang, J. C. Dong, Z. Jiang, J. J. Zhao, J. F. Li, W. S. Yan and M. Wang, *Nat. Commun.*, 2018, **9**, 2885.

Table of Contents Entry

The ternary NiMoCo hybrid nanowire arrays with modulated electrical states and intermediate adsorption energies as efficient water splitting catalysts.

